Biomaterials Science

ROYAL SOCIETY OF CHEMISTRY

PAPER

View Article Online
View Journal | View Issue

Cite this: *Biomater. Sci.*, 2025, **13**, 3958

Iohexol as a refractive index tuning agent for bioinks in high cell density bioprinting†

Yi Xiang,‡[a] Yazhi Sun,‡[a] Jiaao Guan,[a] Tobias Meng-Saccoccio,[a] Ting-Yu Lu,[b] David Berry [c] and Shaochen Chen *[a,b]

Received 17th April 2025,
Accepted 6th June 2025

DOI: 10.1039/d5bm00585j

rsc.li/biomaterials-science

Light-based 3D bioprinting has emerged as a transformative technology for fabrication of biomimetic tissues and artificial organs. High cell density (HCD) bioprinting aims to recapitulate the cellular density and interactions in native tissue, but faces significant challenges in achieving both high resolution and structural fidelity due to light scattering during the photopolymerization process. Refractive index (RI) tuning of the bioink mitigates light scattering to improve printing fidelity. In this study, we developed an iohexol (IHX)-based bioink for digital light processing (DLP) bioprinting. IHX effectively tuned the RI of the bioink to match cellular components to reduce light scattering while still maintaining printability. The bioink demonstrated excellent biocompatibility across multiple cell types, including epithelial, endothelial, parenchymal, and stem cells, while simultaneously supporting post-printing cellular viability, reorganization, and functionality. Using IHX-bioink, we fabricated tubular constructs with lumen diameters ranging from 400 μm to 1.1 mm and utilized strategies to minimize overpolymerization and ensure lumen fidelity. Our results underscore IHX-bioink as a promising biomaterial for scalable, RI-matching 3D bioprinting, enabling the creation of perfusable, HCD constructs for various applications in tissue engineering and regenerative medicine.

1. Introduction

3D bioprinting has emerged as a promising technology for developing artificial organs in tissue engineering and regenerative medicine,[1–3] offering precise deposition of cells and biomaterials to create structures with customized geometries.[4–6] Despite its versatility, a major limitation of bioprinted tissues is the relatively low cell density, often only a few million cells per mL, which falls short of the cell density required for cell–cell interaction and recapitulating native human tissue.[7] This inadequacy impairs critical processes such as paracrine signaling, cell–cell junction formation, and extracellular matrix modeling, all of which are fundamental to biological phenomena such as morphogenesis, polarization, and functionality development.[8–10] Therefore, bioprinting with a high cell density (HCD) that successfully ensures both sufficient cellular content and precise geometrical guidance for cell reorganization would substantially enhance the potential of tissue engineering and biofabrication for *in vitro* tissue modeling and artificial organ production.

However, achieving HCD without compromising cell viability or resolution remains a critical challenge in 3D bioprinting, commonly referred to as the 'cell density/cell viability/resolution' trilemma.[11] In extrusion-based bioprinting, the extrusion process imposes shear stress on HCD bioinks can damage cells,[12,13] while mitigating this stress using a larger nozzle diameter compromises printing resolution.[13] In light-based bioprinting methods, HCD leads to significant light scattering due to the refractive index (RI) mismatch between the cellular components and the surrounding bioink.[14,15] This optical heterogeneity disrupts the light path, deteriorating the resolution and fidelity of the printed constructs.

RI matching bioink has recently emerged as a promising strategy to address this issue in light-based bioprinting.[11,14,16] By tuning the RI of the bioink to closely match that of the cytoplasm, this approach mitigates Rayleigh scattering and improves resolution without compromising cell viability. This strategy has been demonstrated in both DLP bioprinting[11,17] and volumetric bioprinting,[16] two light-based bioprinting techniques that differ in their light propagation distances. DLP bioprinting uses a digital micromirror device (DMD) to project the desired optical pattern of an entire layer onto a vat of

[a]*Department of Chemical and Nano Engineering, University of California San Diego, La Jolla, CA 92093, USA. E-mail: shc064@ucsd.edu*
[b]*Program in Materials Science and Engineering, University of California San Diego, La Jolla, CA 92093, USA*
[c]*Department of Orthopaedic Surgery, University of California San Diego, La Jolla, CA 92093, USA*

†Electronic supplementary information (ESI) available. See DOI: https://doi.org/10.1039/d5bm00585j

‡These authors contributed equally to this work.

bioink, solidifying it layer by layer as the build platform moves upward. By incorporating the biocompatible additive iodixanol (IDX) into a HCD bioink to match its RI to that of cell cytoplasm, the scattering coefficient was reduced from 11.76 mm^{-1} to 0.164 mm^{-1}. This enabled a printing resolution of 50 μm with 0.1 billion cells per mL and the fabrication of perfusable HCD tissues with microscale vascularized lumens that remained viable for 14 days.[11] On the other hand, volumetric bioprinting irradiates the entire bioink volume from multiple angles to simultaneously create an entire 3D object, which requires longer light travel distances. By IDX supplementation, the RI-matched bioink effectively increased ballistic light transmission across the printing volume and expanded the printability window.[16]

To date, IDX remains the only RI-matching additive explored in bioinks. Its success underscores the need to expand the repertoire of reagents to diversify and enhance bioink formulations. In this study, we investigate iohexol (5-[*N*-(2,3-Dihydroxypropyl)acetamido]-2,4,6-triido-*N*,*N*′-bis(2,3-dihydroxypropyl)isophthalamide, CAS: 66108-95-0) as an alternative RI-matching additive for bioinks in light-based bioprinting. Similar to IDX, IHX is an FDA-approved contrast reagent widely used in clinical imaging modalities such as X-ray, computed tomography (CT) and computed tomography angiography (CTA) under the trade name Omnipaque.[18,19] Chemically, IHX is non-ionic, monomeric, and water-soluble, making it suitable for integration with hydrogel-based bioink. With an RI of 1.46 at typical usage concentrations, IHX is comparable to IDX in its optical properties and therefore a promising candidate for RI tuning. Furthermore, IHX offers better versatility in formulation because it is commercially available in its pure form (*i.e.* Histodenz, Nycodenz) that can be prepared into solutions with concentrations exceeding 80% (w/v), equivalent to over 371 mg I mL^{-1}. In contrast, IDX is only available in preformulated solutions with a concentration up to 60% (w/v) or 294 mg I mL^{-1}.[20]

IDX and IHX differ in their osmolarity and structural properties. While IDX is iso-osmolar due to its dimetric molecular structure, IHX has a higher osmolarity from 322 to 844 mOsm kg^{-1}. The higher osmolarity of IHX can cause cytotoxicity from osmotic pressure to the cells during the bioprinting process,[21,22] although it can be completely removed immediately after. Additionally, IHX has a significantly lower molecular weight (821 g mol^{-1}) than IDX (1550 g mol^{-1}), which facilitates faster diffusion during post-bioprinting rinsing and reduces bioink viscosity at equivalent iodine concentrations. These differences highlight the importance to investigate IHX's biocompatibility with various cell types, its optical properties, and compatibility with the bioink formulating and bioprinting processes.

Here, we present for the first time a proof-of-concept study investigating an HCD bioink composed of IHX integrated into a gelatin methacryloyl (GelMA) hydrogel. We characterize its essential properties, including RI, scattering coefficient, viscosity, and printability. Additionally, we evaluate the biocompatibility of the IHX HCD bioink with epithelial, endothelial, parenchymal, and stem cells. Finally, we demonstrate its high-resolution printability by fabricating self-standing HCD perfusable tubes at micrometer-scale and centimeter-scale, the former achieving the highest resolution at this cell density[23,24] and the highest cell density at this resolution[25–29] reported to date by any technique with a wall thickness of 100 μm and cell density of 50 million per mL.

2. Results and discussion

2.1 Reducing light scattering in HCD bioink with IHX

We hypothesized that incorporating IHX into an HCD bioink could tune the RI of the medium to match that of the cytoplasm and thereby reduce light scattering during DLP printing (Fig. 1A). Using 5% (w/v) GelMA as the base bioink (acellular), increasing concentrations of IHX resulted in a progressive increase in the RI of the bioink (Fig. 1B), from 1.34 (0% IHX) to 1.39 (50% IHX) (Fig. 1B). This range closely matches the RI of various cell types, which typically range from 1.36 to 1.39, and supports IHX's potential for RI matching. After measuring the RI of the acellular bioink, 293T cells were added at a concentration of 50 million per mL to the base ink and the corresponding reduced scattering coefficient was measured. As the bioink's RI approached that of 293T cells, the reduced scattering coefficient decreased significantly (Fig. 1C). These results indicate that IHX-bioink can effectively mitigate light scattering (Fig. S1–3†), highlighting its potential to achieve superior fidelity in DLP bioprinting compared to non-RI-matched HCD bioinks.

The incorporation of IHX into the bioink was found to influence the photopolymerization process. 5% (w/v) GelMA (acellular) served as the base bioink to print cylinders 500 μm in height and 500 μm in diameter, increasing the IHX concentrations resulted in a reduction in Young's modulus when the same light intensity and exposure time were applied as shown in Fig. 1D. This suggests a reduced photopolymerization efficiency from the presence of IHX. Importantly, IHX-bioinks remained printable and capable for forming stable constructs as designed under optimized conditions even at the highest concentration of IHX tested. Typically, more light exposure is required to polymerize IHX-containing constructs compared to those without IHX. However, increasing light intensity or exposure time can lead to excessive free radical generation and diffusion, which raise the risk of overpolymerization. To address this, we recommend using base materials with a higher intrinsic photopolymerization rate, such as those with a higher substitution ratio of photopolymerizable groups.[30] These materials can enhance polymerization efficiency, offset the need for excessive light exposure, and minimize the risk of overpolymeriztaion.

The incorporation of IHX slightly increased the viscosity of the bioink at both 25 °C and 37 °C (Fig. 1E and F), while remaining within a range suitable for vat-based polymerization. However, the viscosity remained within the same order of magnitude, ensuring that the bioink's handleability would

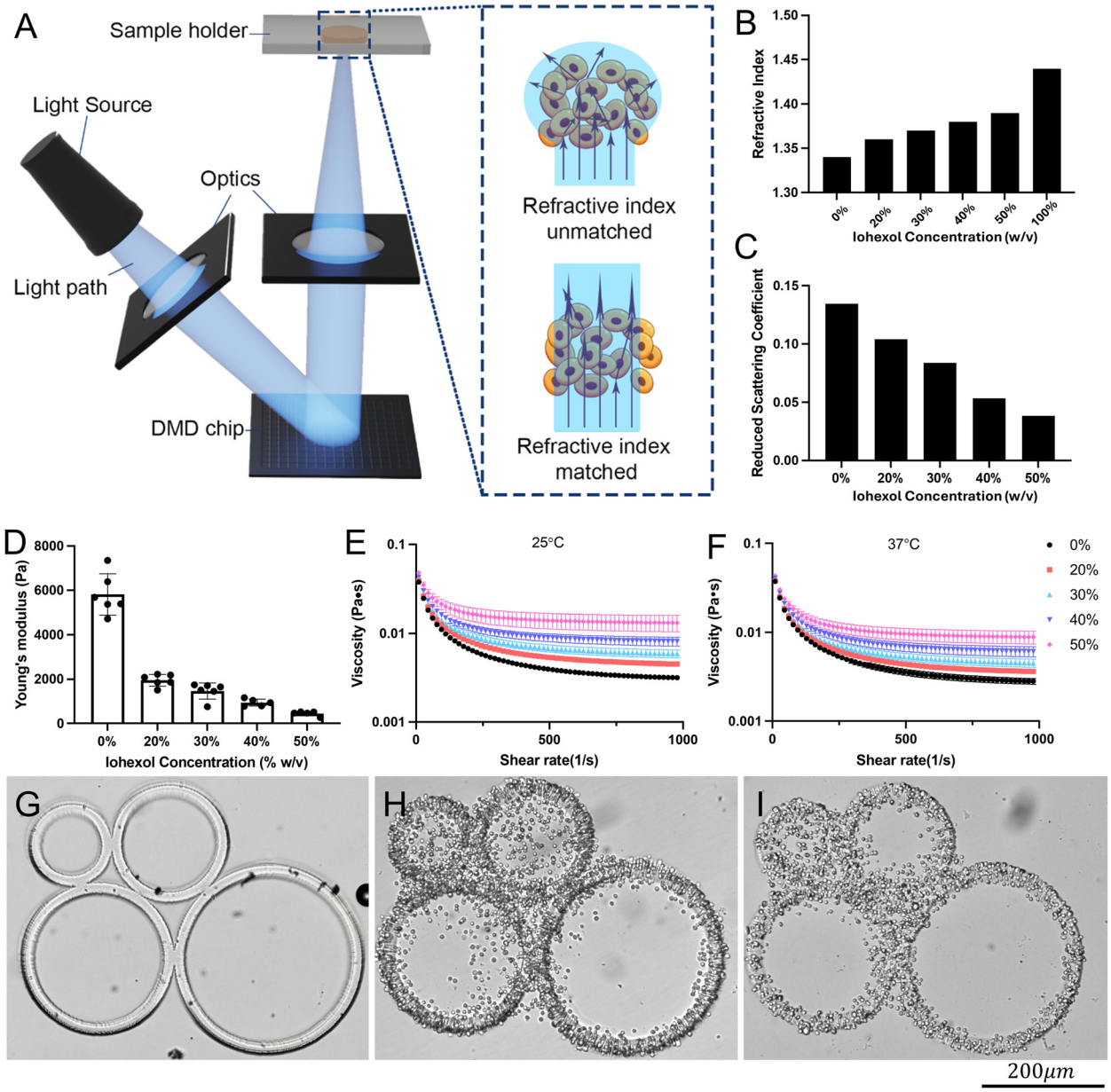

Fig. 1 (A) Schematic of DLP bioprinting using a digital micromirror device (DMD) and light scattering due to refractive index mismatch. (B) Refractive indices of bioinks can be modified by incorporating various concentrations of IHX. (C) Reduced scattering coefficient of HCD bioinks can be reduced by tuning the refractive indices of the bioink to match that of the cells with IHX. (D) Incorporation of IHX in bioink leads to softer constructs. (E) and (F), Incorporation of IHX does not substantially change the viscosity of the bioink and impair its handleability. (G), (H), and I, brightfield images of printed ring structures of acellular bioink (G), HCD non-IHX bioink (H), and HCD IHX-bioink (I) of the sample construct, resulting in different fidelity.

not be compromised during vat polymerization. Notably, IHX contributed less to the bioink's viscosity compared to IDX at the same weight-by-volume concentration for both temperatures,[11] likely due to its smaller molecular weight. Although viscosity does not directly influence printing resolution in DLP systems, a moderate viscosity facilitates practical handling of the bioink.

To evaluate the printing quality of the IHX-bioink, ring structures with a height of 250 μm (corresponding to the typical layer thickness in DLP layer-by-layer printing) were printed. The resolution of cell-free negative feature in each ring of an IHX-bioink with a high 293 cell density of 50 million per mL was compared to an acellular bioink and a 0% IHX bioink at the same cell density. The dimensions of the digital mask design and printed constructs are summarized in Table S1,† and measurement annotation is presented in Fig. S4A.† Briefly, Fig. 1G shows the original pattern printed with a control acellular IHX-bioink, consisting of four circles

with designed diameters of 627, 494, 360, and 227 μm, each with a line width of 40 μm. When printed using a non-IHX HCD bioink (Fig. 1H), the negative features (area without cells) of the 360 μm and 227 μm circles were not resolved, and the cell-free void areas for the 627 μm and 494 μm circles were reduced to diameters of 447 μm and 173 μm, respectively. Compared to non-IHX bioink, the resolution of the HCD features printed with IHX-bioink (Fig. 1I) showed 12.7% improvement for the 627 μm circle, and 37.2% improvement for the 494 μm circle. It produced a cell-free void area with a diameter of 173 μm for the 360 μm circles (48% of designed area), which non-IHX bioink could not resolve. For the smallest circle (227 μm), although the void feature was not fully resolved, a lower density of cells was observed within this area compared to the non-IHX bioink (Fig. 1H and S4A†). Similar results were observed in an independent batch with triplicates (Fig. S4B and Table S2†). In addition, we evaluated the edge sharpness of the printed structures using side-view images. We printed small pillars, each with a height and diameter of 500 μm. As shown in Fig. S5,† both the acellular and IHX-containing bioinks produced solid vertical edges without visible overpolymerization. In contrast, pillars printed with the non-IHX bioink exhibited overpolymerized edges, occupying approximately 13% of the total width of the printed structure. These results suggest that the incorporation of IHX enhances the resolution and fidelity of HCD bioprinting, particularly in resolving small void features, further supporting its potential for high-resolution applications.

In summary, IHX exhibited properties in tuning the RI of HCD bioinks and effectively reduced light scattering, without sacrificing viscosity. Furthermore, IHX-bioinks maintained DLP printability and showed superior print fidelity in comparison to bioink with the same cell density without IHX. Although this study focused on GelMA as a representative hydrogel, our previous work[11] demonstrated IDX – with similar structure and optical properties to IHX – functions effectively in other methacrylate hydrogels such as glycidyl methacrylate hyaluronic acid (GMHA) and alginate methacrylate (AlgiMA). Based on this, we anticipate that IHX would be similarly compatible with a broader range of hydrogel materials, pending optimization of photopolymerization conditions. These results demonstrate IHX-bioink's potential for achieving high-resolution constructs at high cell densities.

2.2 Biocompatibility of IHX-bioink

Although IHX can be fully removed post-wash, its high osmolarity raises concerns about its biocompatibility during the bioprinting process, as transient osmotic stress could compromise cell viability and impair the cell reorganization post-bioprinting. To address these concerns, we evaluated IHX-bioinks with four distinct cell types commonly used in tissue engineering: murine epithelial cell ID8-Defb29/Vegfa (denoted as ID8 below), human umbilical vein endothelial cells (HUVECs), human embryonic stem cell derived cardiomyocytes (ESC-CMs), and human adipose-derived stem cells (ADSCs). Each cell type was mixed with an 50% IHX-bioink containing 50% (w/v) IHX and 5% (w/v) GelMA at a cell density of 50 million per mL and DLP-bioprinted. For comparison, the same cell types were printed using a bioink without IHX (0% IHX) at 5% (w/v) GelMA and a cell density of 50 million per mL. ID8, ESC-CMs, and ADSCs were printed in a pie-shaped to achieve 3D encapsulation, and HUVECs were printed in donut shapes to facilitate their monolayer formation.

For all the four cell types, Live/Dead staining (Fig. S6†) demonstrated a majority of cells remained viable immediately after bioprinting in both 50% IHX and 0% IHX bioinks with minimal cell death. After 1 day of culture, ID8, ESC-CM, and ADSC cells maintained high viability regardless of the bioink composition. In HUVEC samples, cell migration to the edges of the constructs was observed in both 50% IHX and 0% IHX samples. Notably, in the 0% IHX samples, some cells remained entrapped in the center of the construct which led to necrosis, whereas no dead cells were observed in the 50% IHX samples. This difference may be attributed to the softer matrix in the 50% IHX bioink, which enabled HUVEC migration to the surface.

In summary, the incorporation of IHX did not induce acute cytotoxicity to compromise cell viability during bioprinting. The post-bioprinting reorganization and functionalization of the HCD constructs were further investigated by immunofluorescence staining of cell-specific biomarkers.

ID8-Defb29/Vegfa is a murine ovarian epithelial cell line used to model high grade serous ovarian cancer (HGSOC) progression in syngeneic mouse models and complex *in vitro* models.[31,32] After 1 day of culture, ID8 cells in the center of the pie-shaped construct reorganized into spheroids in both 50% IHX and 0% IHX bioinks (Fig. S7a†). The spheroids stained positive for E-Cadherin (E-Cad) on the surface which co-localized with F-actin, indicating the establishment of cell–cell interaction and epithelial phenotype. By day 3, ID8 cells at the pie's edge also expressed E-Cad in both bioink conditions (Fig. 2a). However, while spheroids in the center of the 0% IHX bioink retained their distinct organization, those in the 50% IHX bioink merged into a large, continuous organization, with a notable number of cells migrating out of the pie construct. This behavior is likely attributed to the softer matrix provided by the 50% IHX bioink, which facilitated cellular movement and reorganization.

HUVECs are the most widely used endothelial cells in *in vitro* vasculature engineering.[33–35] Since HUVECs grow into a monolayer on the substrate, geometrical cues are critical to guide their assembly. When bioprinted in the 0% IHX and 50% IHX bioinks, HUVECs migrated to the surface of the donut-shaped constructs by day 4, showing an elongated morphology and aligning long the boundary. CD31, a marker of tight junctions, was expressed under both bioink conditions and indicated successful vascularization (Fig. S7b†). By day 10, the prints differed in their CD31 expression. The 50% IHX construct demonstrated tight junctions which fully covered both the inner and outer boundaries (Fig. 2b). In contrast for the 0% IHX bioink, CD31 were observed only in the outer circle, while the inner circle exhibited minimal coverage. This discre-

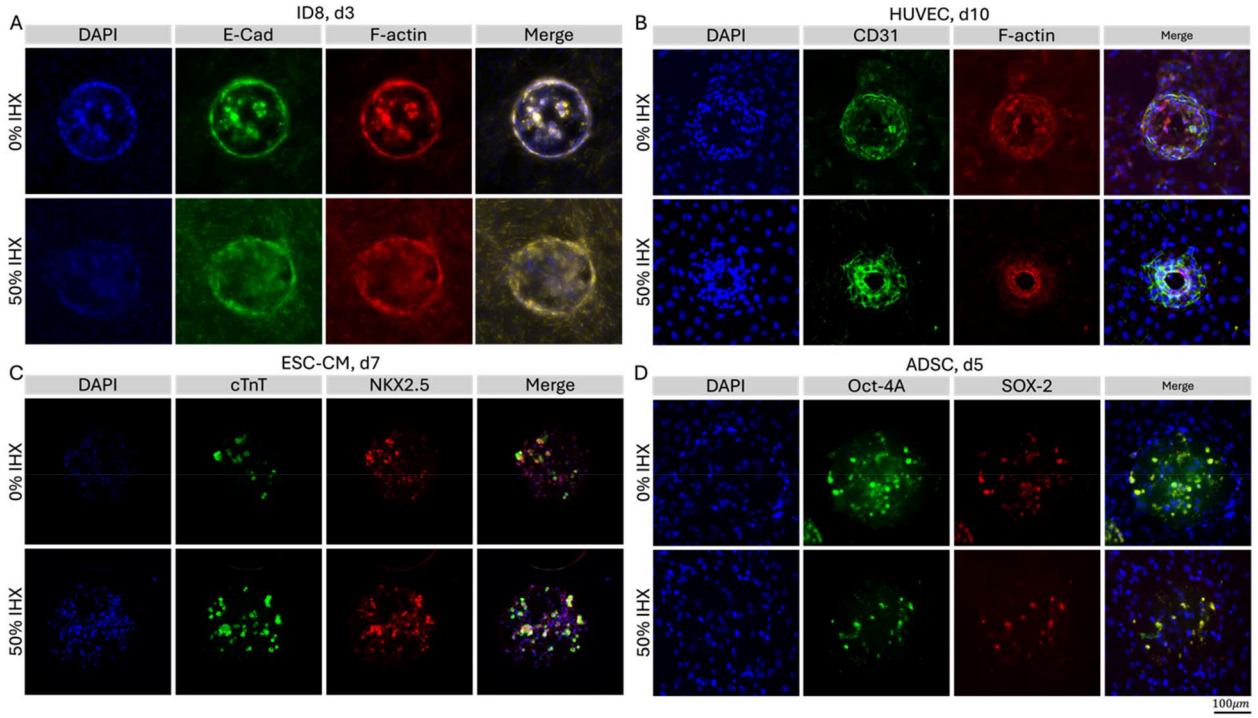

Fig. 2 Immunofluorescence images demonstrating cell recovery and reorganization after bioprinting in IHX-bioink at designated biologically-relevant time points. (A) Murine epithelial cell ID8-Defb29/Vegfa (denoted as ID8) after 3 days. (B) Human umbilical vein endothelial cells (HUVEC) after 10 days. (C) Human embryonic stem cell derived cardiomyocytes (ESC-CMs) after 7 days. (D) Human adipose-derived stem cells (ADSCs) 5 days.

pancy can be attributed to overpolymerization in the non-IHX bioink, which failed to create a clear boundary in the inner circle to support HUVEC reorganization due to light scattering. In comparison, the incorporation of IHX improved the bioprinting fidelity, providing a well-defined surface which facilitated the formation of continuous tight junctions on both boundaries.

ESC-CMs are cardiac parenchymal cells which serve as an essential cell source in cardiac tissue engineering,[36] including heart-on-a-chip systems and cardiac patches. ESC-CMs typically require 4–7 days to recover from dissociation and regain contractility following bioprinting. Immunofluorescence staining revealed cardiac troponin (cTnT) expression, a marker of cardiac contractile function, in ESC-CMs on day 4 in both 50% IHX and 0% IHX bioinks, particularly in the regions where cells had organized into clusters (Fig. S7c†). Additionally, many cells stained positive for NKX2.5, a cardiac lineage marker, but lacked cTnT expression, suggesting they remained viable but had not yet regained contractile function. By day 7, the 50% IHX bioink supported a higher number of cTnT-positive clusters compared to the 0% IHX bioink, in which more cells remained NKX2.5-positive but cTnT-negative. These results suggest that the incorporation of IHX did not hamper the ESC-CM reorganization and functional recovery post-bioprinting. Instead, the softer matrix it created facilitated cardiac contractile function.

ADSCs are a highly abundant and multipotent cell source, and they are widely used in tissue engineering for their ability to differentiate into multiple cell types.[37] Immunofluorescence staining demonstrated that on day 1, ADSCs remained positive for stemness marker Oct-4A in both 50% IHX and 0% IHX bioinks, with slightly higher marker retention in the 0% IHX bioink (Fig. S7d†). By day 5 (Fig. 2d), many ADSCs in the 50% IHX constructs had migrated out of the pie construct and lost Oct-4A expression, whereas those in the 0% IHX bioink largely retained marker expression. However, in 50% IHX bioink, ADSC aggregates remained positive for Oct-4A. Moreover, an increased number of cells stained positive for SOX-2, a stemness marker co-expressed with Oct-4A, than on day 1. This suggests that while IHX incorporation initially impacts ADSC stemness, the loss of SOX-2 is partially reversible over time. These findings indicate the compatibility of IHX bioink with ADSC while highlighting the need for optimization of bioink formulations to better preserve ADSC stemness. Tailoring post-printing culture conditions and differentiation timeline will also be critical to meet specific tissue engineering requirements.

In summary, IHX demonstrated biocompatibility with all 4 cell types investigated, suggesting its broader applicability for other cell types. Compared to non-IHX bioinks, IHX incorporation did not compromise cell viability or hinder cellular reorganization post-bioprinting; it was able to facilitate the fabrication of the geometrical design to support cellular reorganization. However, bioprinting parameters and post-printing culture conditions should be tailored to the specific characteristics of each cell type and the study's objectives. With its

ability to improve bioprinting resolution, IHX shows significant potential as an additive for HCD bioink formulation in tissue engineering.

2.3 High-fidelity HCD bioprinting of IHX-bioink

Achieving high-resolution bioprinting with HCD bioinks demands precise control over structural fidelity and mechanical stability. To assess the performance of IHX-bioink in such applications, we fabricated a perfusable micro-scaled tube using DLP bioprinting. The tube had an inner diameter of 400 μm, an outer diameter of 600 μm, and a length of 3 mm, encapsulating 50 million per mL 293T cells or ADSCs. For both cell types, bioinks with an IHX concentration of 45% were used.

The bioprinting process followed the microscale continuous optical printing (μCOP) method.[38] Specifically, a transverse plane mask of the tube was optically projected onto the HCD IHX-bioink reservoir, while a probe, serving as the fabrication substrate, moved along the *z*-axis to guide the extrusion and achieve the desired tube length (Fig. 3a). The resulting tube featured a lumen capable of accommodating a 0.2 mm diameter stick (Fig. 3b), suggesting its potential for perfusion with a similarly sized needle. Differential interference contrast (DIC) imaging revealed a well-defined lumen in both the side (Fig. 3c) and the transverse plane (Fig. 3d) views. DAPI-stained samples further confirmed HCD within the printed structure, visualized as cell nuclei uniformly distributed throughout the construct (Fig. 3e and f).

Successful fabrication of the tube requires careful consideration of several factors. First, sufficient rigidity of the printed material was essential to maintain structural integrity during the bioprinting process. HCD materials are inherently soft, making the printed construct prone to deformation or collapse under its own weight, which could result in misalignment with the fabrication surface during printing. Second, minimizing the total printing time was critical to prevent overpolymerization within the lumen. Free radicals generated during photoinitiation can persist and diffuse into the unexposed regions,[39] leading to unintended polymerization and lumen clogging over extended printing time.

To address these challenges, we implemented several key modifications to the bioink and printing protocol. First, the GelMA concentration was increased to 7.5% (w/v) to enhance the rigidity of the printed construct, reducing deformation during printing. Second, 1% (w/v) PEGDA700 was added to provide abundant acrylate groups, accelerating the polymerization rate and reducing the required light exposure time. Third, to mitigate overpolymerization in the lumen, 0.01% (w/v) tartrazine, a photoabsorber, was incorporated to limit free radical generation outside the designated light-exposure region. Finally, a 30% grayscale setting was applied to the mask, leveraging the DMD chip's ability to toggle off for 30% of the exposure time and thereby reduce excessive free radical generation. These modifications collectively enabled the successful and reproducible fabrication of the perfusable micro-scaled HCD tube.

The printing parameters required further optimization to accommodate the unique characteristics of each different cell type. For example, ADSCs are larger in volume compared to 293T cells, and therefore the photopolymerization rate of the bioink encapsulating ADSCs with a similar cell density as 293T is slower. To successfully bioprint HCD micro-tubes encapsulating 50 million ADSCs, we reduce the grayscale to 20% and decreased the printing speed to allow for longer light exposure.

After printing, the tube was fixed later that day and stained for nuclei (DAPI) and stemness markers (SOX-2 and Oct-4). The sample was sectioned and scanned through the horizontal plane using a confocal microscope, and the images were used for 3D reconstruction (Fig. 4). The results confirmed that a high density of ADSC cells was encapsulated within the printed tube, and the expression of the stemness markers was maintained. This suggests the potential of the HCD ADSC tube for differentiation into various cell types, including adipocytes, chondrocytes, osteoblasts, or Schwann-like cells, for tissue engineering applications. Additionally, the lumen offers opportunities for co-culture, such as with endothelial cells or neural cells, expanding its versatility.

This achievement represents a state-of-the-art milestone in bioprinting of tubular constructs, demonstrating the highest resolution at this cell density and the highest cell density at this resolution reported to date by any technique with a wall thickness of 100 μm and cell density of 50 million per mL. These results underscore the potential of IHX-bioink to advance tissue engineering by enabling precise and scalable fabrication of complex, high-cell-density constructs.

2.4 HCD bioprinting of a physiologically relevant-size construct with IHX-bioink

IHX-bioink is also capable of DLP bioprinting larger HCD constructs with physiologically relevant dimensions, as demonstrated by fabricating a larger tube with an inner diameter of 1.1 mm, an outer diameter of 2 mm, and a length of 9 mm, encapsulating 50 million per mL 293T cells (Fig. 5A). This dimension is comparable to the isthmus region of a fallopian tube.

Tubular constructs of or beyond this size are particularly challenging to fabricate *via* processes such as DLP printing and stereolithography 3D printing due to the risk of cupping blowout, a phenomenon where negative pressure during printing causes deformation or collapse of the hollow lumen structure,[40] which is especially likely when using soft materials like HCD bioinks. To avoid this, we employed a layer-by-layer printing strategy. A mask of the transverse plane of the tube was projected onto the HCD IHX-bioink vat, and the probe served as the fabrication substrate. However, unlike continuous printing, light switches on and off for each printing layer in repeated cycles throughout the process. During the intervals when the light was off, the probe was lifted 1 cm above the vat, allowing the printed lumen to connect to external air and release negative pressure and the bioink to flow in to replace the polymerized hydrogel.

Due to the length of the designed tube and the layer-by-layer strategy employed, the total printing time was relatively

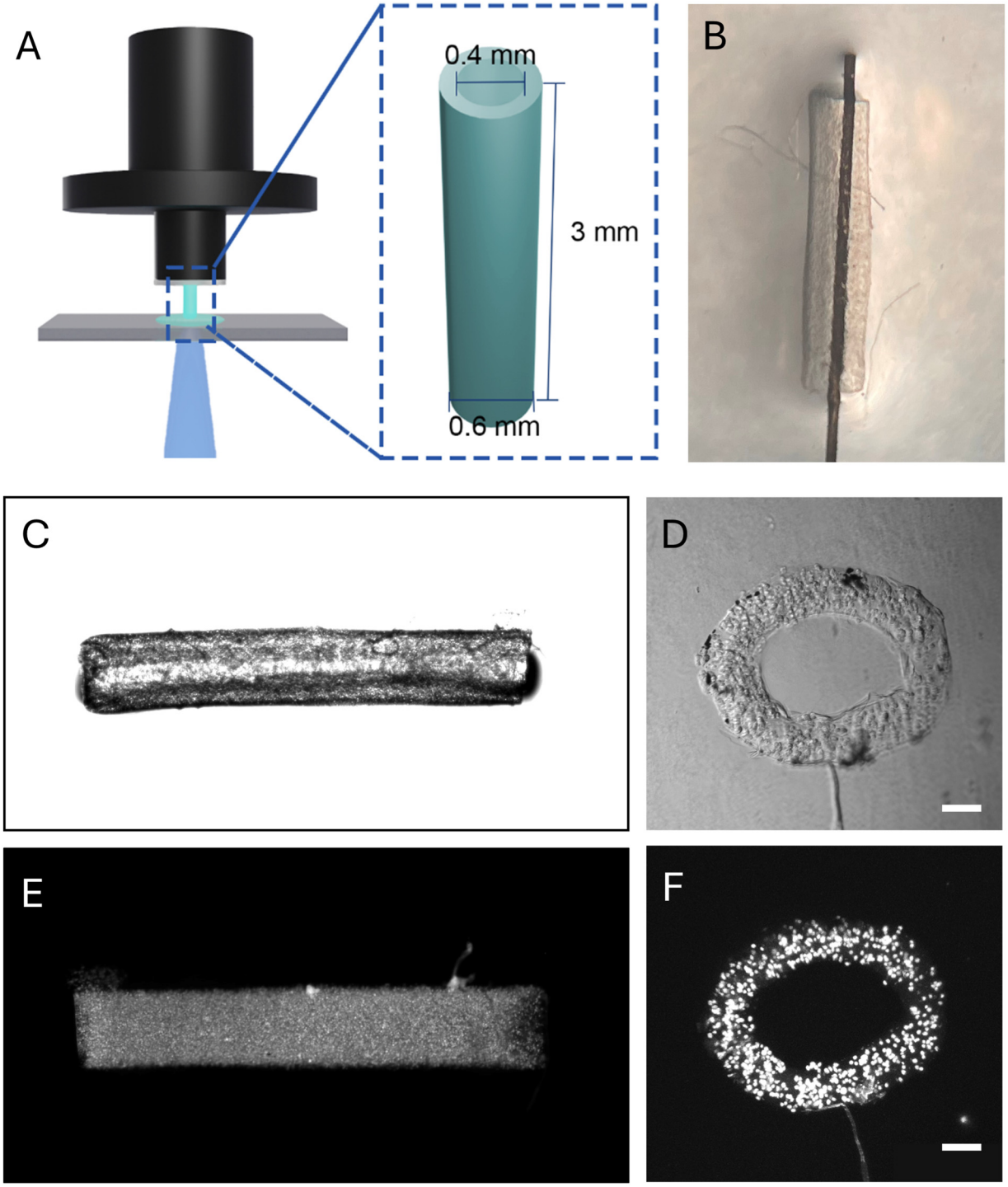

Fig. 3 Bioprinting of an HCD micro-tube. (A) Schematic of the printing set-up and dimensions of the HCD tube. (B) The lumen of the tube allows a stick (diameter = 0.2 mm) to pass through. (C) and (D) DIC image of the tube (C: side view, D: traverse plane). (E) and (F) Fluorescence image of the tube stained with DAPI (E: side view, F: traverse plane). Scale bars: (B) 1 mm, (C) and (E) 500 μm, (D) and (F), 200 μm.

long. As with microscale tubes, the lumen was subjected to a higher risk of overpolymerization and clogging due to prolonged exposure to free radicals. To address this, we employed a multi-segment approach. After printing several layers (a segment), we paused the process, removed the sample and the probe from the vat, rinsed away any residual material, and then resumed printing. This approach effectively minimized lumen clogging and ensured the successful fabrication of the physiologically relevant-size HCD tube.

Using this method, we were able to print a large and perfusable HCD tube (Fig. 5B). The lumen was clearly visible in the DIC images of both the side (Fig. 5C) and the transverse plane

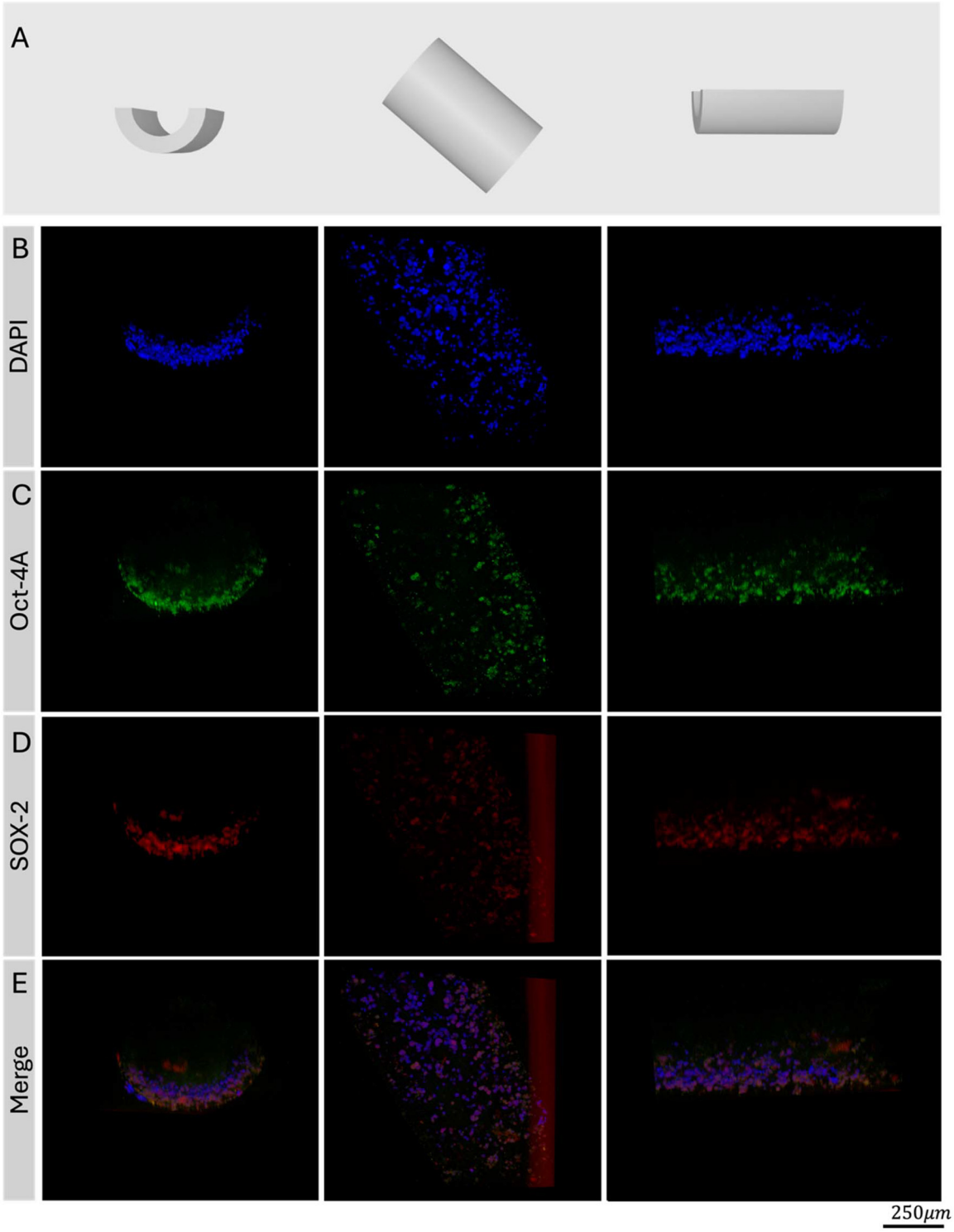

Fig. 4 3D reconstruction of the HCD micro-tube encapsulating ADSC from confocal microscopic imaging. (A) Schematic of the tube section imaged (left: front; middle: top; right: side). (B) Immunofluorescence staining results of DAPI, (C) Oct-4A, and (D) SOX-2 of the tube. In left and right panels of SOX-2 and merge images (E), a reflection artifact outside the sample region was digitally removed for clarity.

views (Fig. 5D). The tubes were also stained with DAPI to visualize the nuclei, confirming that the HCD remained encapsulated in the printed part (Fig. 5E and F).

It is notable that at this scale, bioprinting an HCD tube is feasible with alternative approaches, such as co-axial extrusion printing, which uses a sacrificial material in the inner nozzle

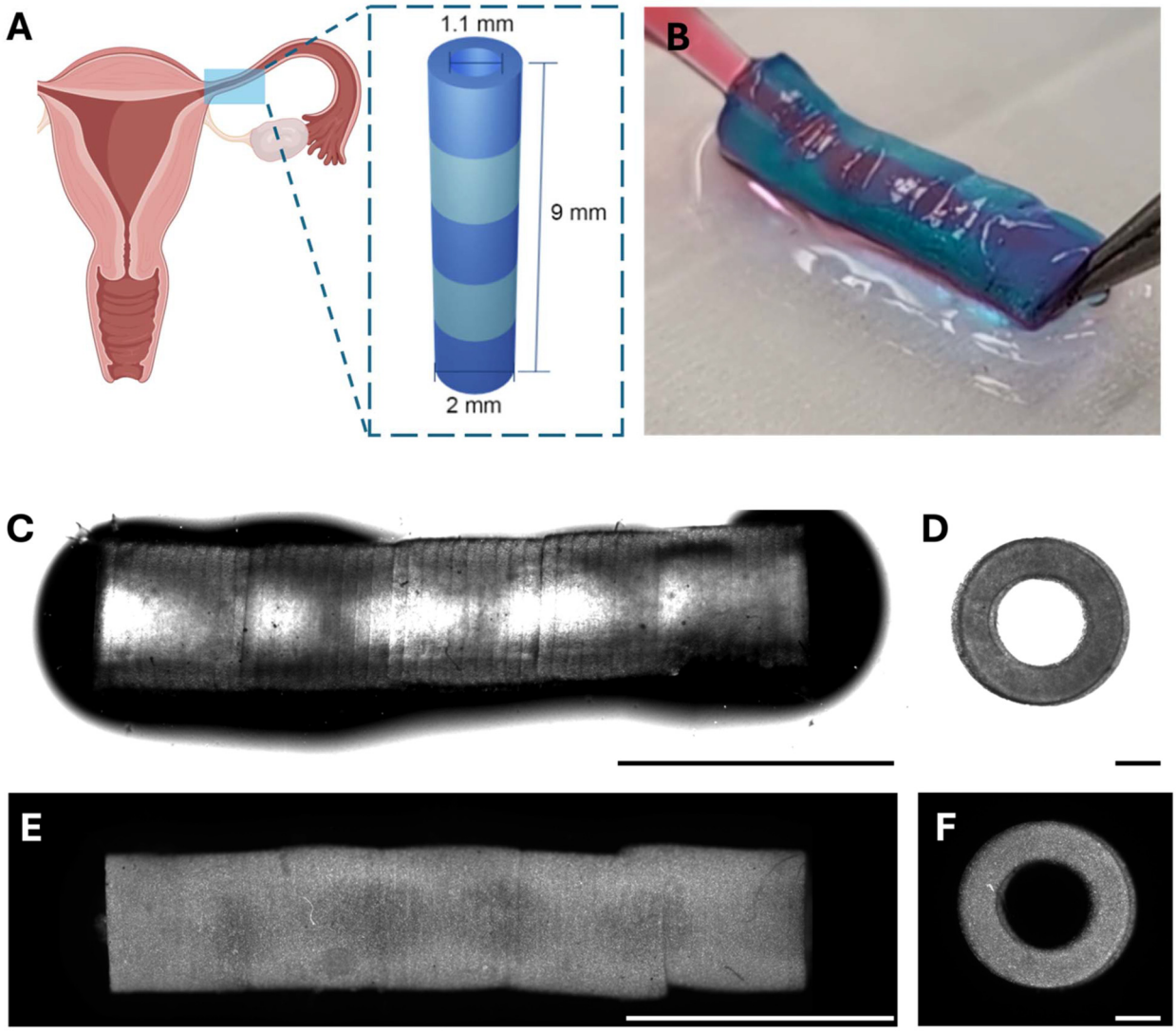

Fig. 5 Bioprinting of an HCD tube with a physiologically relevant size. (A) The dimension of the HCD tube is comparable to the isthmus region of a fallopian tube. (B) The HCD tube is perfusable (the perfusing solution was stained with red food dye and tube stained with blue food dye for clarity). (C) and (D) Differential interference contract (DIC) image of the tube (C: side view, D: traverse plane). (E) and (F), fluorescence image of the tube stained with DAPI (E: side view, F: traverse plane). Scale bar: C and E, 3.6 mm. D and F, 500 μm.

and HCD bioink in the outer nozzle.[28] Compared to the DLP method, the extrusion method offers several advantages, including faster operation, reduced labor intensity, the ability to print longer tubes, and the flexibility to fold tubes into various shapes to meet engineered design requirements. However, even at this feature size, the cells will experience high shear stress due to the extrusion, and therefore the DLP method would be preferrable for shear-sensitive cell types or studies. It is also notable that the lumen printed using the DLP method exhibited some non-uniformity, characterized by an undulating surface associated with the beginning and end of each segment. This is caused by overpolymerization during post-exposure, as well as the misalignment of the end of the large tube due to the softness of the material. While further optimization of the printing procedure could improve lumen uniformity, it may not completely eliminate these surface irregularities. Interestingly, such textures resemble the organic undulating surfaces of natural lumens, such as those found in arteries and intestines, and would be challenging to replicate using extrusion printing.

At this scale, RI matching is also not the sole viable strategy for lumen fabrication in DLP bioprinting. Alternative methods, such as optimizing printing parameters or modifying the optical masks to compensate for light scattering using machine learning,[15,41] may also mitigate the cell light scattering effect. These approaches could eliminate the need for RI-matching additives, which may impact cellular signaling. Nevertheless, we recommend incorporating IHX or IDX for two major reasons. First, RI-matched bioink facilitate uniform photopolymerization by minimizing light scattering in HCD

bioink, which leads to enhanced structural fidelity and to resolve challenging prints, one example being the microtubules. Second, IHX incorporation reduces the trial-and-error optimization process, which is particularly advantageous given the substantial number of cells required for HCD constructs of this size. Thus, IHX improves the structure of the construct and reduces time and wasted material.

In summary, we demonstrated that IHX-bioink enables the bioprinting of tubular constructs with channel diameters ranging from 400 μm to 1.1 mm. This achievement advances the integration of RI-matching strategy with DLP bioprinting techniques to recapitulate structures of biological systems. While achieving the smallest dimensions highlights the precision of our approach, the RI-matching DLP bioprinting strategy developed for larger constructs minimizes shear stress on cells and enables the fabrication of organic, undulating textures on the lumen surface without additional configurations, compared to extrusion-based bioprinting methods. These capabilities expand the potential for fabricating complex, perfusable tissue constructs suitable for applications in disease modeling, drug testing, and regenerative medicine.

3. Conclusion

This study established IHX-based bioink as an effective biocompatible additive for RI matching in HCD bioprinting. By reducing light scattering while maintaining printability, IHX-bioink enabled the high-fidelity fabrication of biomimetic constructs across high-resolution and physiologically relevant scales. The bioink demonstrated compatibility with diverse cell types, supporting post-printing viability and cellular reorganization. These results demonstrate IHX-bioink as a versatile and robust platform for advancing tissue engineering, disease modeling, and regenerative medicine by enabling precise bioprinting of complex constructs with a high cell density.

4. Experimental section

4.1 Materials

IHX powder was purchased from Thermo Fisher Scientific (Cat.# 466650250). PEGDA700 was purchased from Sigma-Aldrich (Cat.# 45508). Tartrazine was purchased from Sigma-Aldrich (Cat.# T0388). Lithium phenyl(2.4.6-trimethylbenzoyl) phosphinate (LAP) was purchased from TCI (Cat.# L0290). Dulbecco's phosphate-buffered saline (DPBS) was purchased from Gibco (Cat.# 14190). Sodium azide was purchased from Alfa Aesar (Cat.# 14314).

GelMA85 was synthesized in-house from type A gelatin (Cat.# G2500, Sigma-Aldrich) and methacrylic anhydride (MA, Cat.# 276685, Sigma-Aldrich) in DPBS. A 10% (w/v) gelatin solution in DPBS was first prepared and heated to 60 °C. MA was added to the gelatin solution dropwise at a ratio of 0.8 mL MA per gram gelatin. The reaction was kept at 60 °C for 3 h, and then quenched by diluting 2 times with DPBS preheated to 60 °C. The product was purified by dialyzing against MilliQ water at 37 °C for 7 days, vacuum filtered. The purified product was lyophilized for 3 days and stored in −20 °C in dark until use.

GelMA95 (PhotoGel ~95%) was a gift from Cellink (Advanced Matrix Cat.# 5208).

4.2 Cell culture

293T cell line was obtained from ATCC (CRL-3216). The cells were maintained and propagated in a complete medium consisting of 90% (v/v) Dulbecco's Modified Eagle Medium (DMEM, Gibco Cat.# 11965118) and 10% (v/v) fetal bovine serum (FBS, HyClone Cat.# SH30396.03HI) supplemented with 1× Penicillin–Streptomycin (Cat# P4333, Sigma-Aldrich). The cells were disassociated by incubating with 0.25% trypsin-EDTA (Gibco Cat.# 25200056) for subculture or bioprinting.

ID8-Defb29/Vegfa cells (ID8) were maintained and propagated in RPMI 1640 medium (Cat# 11875093, Gibco) supplemented with 1 mM sodium pyruvate (Cat# 11360070, Gibco), 1 mM 2-mercaptoethanol (Cat.# 21985023, Gibco), 10% (v/v) FBS and 1× Penicillin–Streptomycin. The cells were disassociated by incubating with 0.25% trypsin-EDTA for subculture or bioprinting.

Primary human umbilical vein endothelial cells (HUVEC) were maintained and propagated in endothelial cell growth medium (Cat.# 211-500, Cell Applications, Inc.). The cells were disassociated by incubating with 0.25% trypsin-EDTA for subculture or bioprinting.

Human embryonic stem cell derived cardiomyocytes and their maintenance medium were a kind gift from Prof. Neil Chi Lab at the University of California, San Diego. Upon recipient, the cells were disassociated with collagenase IV (Gibco Cat.# 17104019) for bioprinting.

Primary human adipose-derived stem cells were maintained and propagated in human mesenchymal stem cell growth medium (Cat.# 419-500, Cell Applications, Inc.). The cells were disassociated by incubating with 0.25% trypsin-EDTA for subculture or bioprinting.

293T cells and ID8 cells were subcultured at a ratio of 1 : 3 every 2 days. HUVECs and ADSCs were subcultured at a ratio of 1 : 3 when reach 70% confluency (3–5 days).

Disassociated cells were sampled for trypan blue staining (Gibco Cat.# 15250061) to determine the cell number and viability. Only cells with ≥99% live cells were proceeded for bioprinting.

Immediately after bioprinting, all the cellular constructs for biocompatibility investigation in section 2.2 were rinsed with 1 mL DPBS for 3 times to remove excessive material and IHX and LAP residue. The microscale cellular tubes printed in section 2.3 were perfused with 200 μL DPBS for 3 times and rinsed with 1 mL DPBS on the exterior for 3 times. For the millimeter scale cellular tubes printed in section 2.4, the constructs were rinsed with 1 mL DPBS for 3 times immediately after printing of each segment. After rinsing, all the cellular constructs were cultured in the respective medium per their cell type until examination time point. All the cells and cellular

constructs were cultured in a humidified incubator at 37 °C, 5% CO_2.

4.3 Bioink composition

Stock solutions of each component of the bioink were prepared. GelMA85 or GelMA95 were dissolved in DPBS to 20% (w/v); LAP was dissolved in DPBS to 4% (w/v); tartrazine was dissolved in DPBS to 1% (w/v); IHX was dissolved in DPBS to 80% (w/v). All the solutions were filtered through a 0.22 μm membrane to ensure sterility and homogeneity. The solutions were kept in 4 °C in dark and replenished every 3 months.

For characterization studies in section 2.1 and biocompatibility investigation in section 2.2, the stock solutions and DPBS were combined to reach a final solution of 5% (w/v) GelMA85, 0.6% (w/v) LAP, and IHX concentrations as designated.

For microscale cellular tubes printed in section 2.3, the stock solutions and DPBS were combined to reach a final solution of 7.5% (w/v) GelMA95, 0.6% (w/v) LAP, 0.01% (w/v) tartrazine, and 45% (w/v) IHX, supplemented by PEGDA700 to a final concentration of 1% (w/v).

For millimeter scale cellular tubes printed in section 2.4, the stock solution and DPBS were combined to reach a final solution of 7.5% (w/v) GelMA95, 0.6% (w/v) LAP, 0.01% (w/v) tartrazine, and 45% (w/v) IHX.

The bioinks were mixed well by pipetting with a 1 mL pipette. For cellular bioprinting, cells were pelleted and resuspended with the bioink to reach the designated cell density. 293T, ID8, and HUVECs were pelleted by centrifuging at 300*g* for 5 minutes. ESC-CMs and ADSCs were pelleted by centrifuging at 200*g* for 5 minutes.

Acellular bioinks were prepared from the stock solutions on the same day of bioprinting; cells were added to the bioinks immediately prior to bioprinting per the cell density specified for each application.

4.4 Bioprinting

All samples were printed with a custom-built DLP bioprinter. During the printing process, an LED light with a wavelength of 385 nm was reflected by a digital micromirror device (DMD) chip to project the designed pattern onto the focus plane, where the sample holder was positioned. For the prints in Fig. 1 and 2, the bioink was loaded into the gap with a height of 500 μm between a methacylated coverslip and a PDMS sheet. Samples were printed under a static light exposure with a power of 32 mW cm^{-2} for 20 seconds.

For 3D small tubes in Fig. 3 and 4, continuous printing was applied. A vertically movable probe was placed right on the focus plane, with a methacrylated coverslip glued onto the surface. During printing, the probe kept moving up continuously from the position attaching the bioink reservoir to the designed height at a constant speed, while a ring-shaped mask was projected to the focus plane. The thin layer of bioink that the light passed through was photocrosslilnked. As the probe lifted up, the small tube was constructed with the first printed part attached to the coverslip. After the printing was completed, the printed small tube was rinsed to remove uncrosslinked bioink, then was cut off from the coverslip with a blade.

For the 3D HCD construct in Fig. 5, a layer-by-layer approach was used. The probe was lifted up to 0.2 mm above the focus plane, and the light was on to cure this thin layer of bioink. The light was turned off, and the probe moved up to 1 cm, then moved down to 0.2 mm above the previous position for printing the next 0.2 mm layer. This up-and-down motion allowed the lumen in the printed tube to connect to the external air, and allow the bioink to flow and refill, preventing the hollow cavities due to the lack of bioink. A single layer-by-layer printing session was used to print a segment with a height of 1.8 mm. After each segment was printed, the probe was taken off and the printing was rinsed to remove the uncrosslinked bioink, preventing overpolymerization and clogging in the lumen.

4.5 Scattering measurement and simulation

Scattering measurement was conducted using the method and code established in the previous publication.[11] Briefly, the refractive index was measured by Hanna HI96801 digital refractometer. The angular intensity distribution of the scattered light at 385 nm was measured with a homemade optical goniometer type setup. The light intensity of scattered light at different angles was measured with a light power meter (Thorlabs). Six replicates of 1 mm-thick samples and two replicates of 250 μm-thick samples containing 50 million cells per ml were measured for each IHX concentration. The total transmittance and total reflectance at 385 nm were measured using an Ultraviolet–Visible-Near infrared (UV-Vis-NIR) spectroscope (PerkinElmer, Lambda 1050) with an integrating sphere. Three replicates of glass slides holding 1 mm-thick bioink containing 50 million cells per ml were measured for each IHX concentration. Monte Carlo (MC) simulation and particle swarm optimization were used to calculate the scattering coefficient. The total transmittance was also used in MC simulation and optimization to calculate the optical properties. By incorporating two sample thicknesses for angular intensity measurement instead of the one-thickness in the previous publication, we were able to resolve a more reliable set of scattering coefficient, absorption coefficient, and anisotropy for each IHX concentration.

4.6 Mechanical characterization

Young's moduli of the printed structures with different IHX concentrations were measured with a MicroSquisher (CellScale). DLP-printed cylinders with a diameter of 1 mm and a height of 1 mm were printed for testing. The printed cylinder sample were placed under a platen and was compressed to a magnitude of 200 μm at a speed of 8 μm s^{-1}, then recover at the same speed. Each sample was compressed three times. The first two cycles removed hysteresis caused by internal friction. Three replicates were measured for each IHX concentration. Compressive modulus was calculated from the data of the third cycle by utilizing customized MATLAB scripts.

The rheological properties of GelMA bioinks were assessed using a rotational rheometer (Discovery Hybrid Rheometer HR 30, TA Instruments), fitted with a 40 mm diameter cone geometry at a 2° angle and a temperature-controlled Peltier plate. A 52 μm gap was maintained between the cone tip and the Peltier plate for all measurements. Viscosity was recorded across a shear rate range of 1 to 1000 s^{-1} in flow ramp mode, with three technical replicates for each IHX concentration.

4.7 Staining and imaging

Live/dead staining was performed with Calcein AM (Cat.# C3099, Invitrogen) and propidium iodide (Cat.# P3566, Invitrogen). A staining solution consisted of 1 μg mL^{-1} Calcein AM and 5 μg mL^{-1} propidium iodide in DPBS. At designated time point, the cellular constructs were rinsed with 1 mL DPBS for 3 times and incubated with the staining solution in a humidified incubator at 37 °C, 5% CO_2 for 20 minutes. The constructs were rinsed with 1 mL DPBS for 3 times after staining and imaged immediately using a Leica DMI 6000B fluorescent microscope.

Immunofluorescence staining was performed following fixation (4% paraformaldehyde for 15 minutes at 4 °C, Cat.# J19943.K2, Thermo Fisher Scientific) and penetration (Triton X-100 diluted to 0.2% (w/v) in DPBS, 10 minutes at room temperature, Cat.# T8787, Sigma-Aldrich) using cell staining buffer (Cat.# 420201, Biolegend). Antibody specification, dilution, and incubation conditions are provided in ESI Table S1.†

Microscale and millimeter scale tubes with 293T cells were manually sectioned through the traverse plane for imaging of Fig. 3d, f and 5d, f under a stereomicroscope. To facilitate handling, the tubes were encapsulated in a 2% agarose cube, and platinum-coated double-edged razor blades were used for precise cutting.

Brightfield, DIC, and fluorescence imaging were performed on Leica DMI 6000B fluorescent microscope.

Microscale ADSC tubes were imaged on Leica SP8 confocal system. 3D reconstruction was performed using the Leica LAS X software.

Conflicts of interest

There are no conflicts to declare.

Data availability

The data supporting this article have been included as part of the ESI.†

Acknowledgements

This work is supported in part by a grant (R01HD112026) from the National Institutes of Health and grant from the National Science Foundation (2135720 and 2223669). We thank Cellink for donating the commercial grade GelMA bioinks. We thank the UCSD School of Medicine Microscopy Core, which is supported by an NINDS P30 grant (NS047101), for the use of their confocal microscopes. We also thank Ashley Altera for her help with the manuscript.

References

1 Y. Ma, B. Deng, R. He and P. Huang, Advancements of 3D bioprinting in regenerative medicine: Exploring cell sources for organ fabrication, *Heliyon*, 2024, **10**, DOI: 10.1016/j.heliyon.2024.e24593.

2 Y. G. Jeong, J. J. Yoo, S. J. Lee and M. S. Kim, 3D digital light process bioprinting: Cutting-edge platforms for resolution of organ fabrication, *Mater. Today Bio*, 2024, **29**, 101284, DOI: 10.1016/j.mtbio.2024.101284.

3 G. Huang, Y. Zhao, D. Chen, L. Wei, Z. Hu, J. Li, *et al.*, Applications, advancements, and challenges of 3D bioprinting in organ transplantation, *Biomater. Sci.*, 2024, **12**, 1425–1448, DOI: 10.1039/d3bm01934a.

4 W. Lv, H. Zhou, A. Aazmi, M. Yu, X. Xu, H. Yang, *et al.*, Constructing biomimetic liver models through biomaterials and vasculature engineering, *Regener. Biomater.*, 2022, **9**, rbac079, DOI: 10.1093/rb/rbac079.

5 P. Soman, B. T. D. Tobe, J. W. Lee, A. M. Winquist, I. Singec, K. S. Vecchio, *et al.*, Three-dimensional scaffolding to investigate neuronal derivatives of human embryonic stem cells, *Biomed. Microdevices*, 2012, **14**, 829–838, DOI: 10.1007/s10544-012-9662-7.

6 S. H. Pyo, P. Wang, H. H. Hwang, W. Zhu, J. Warner and S. Chen, Continuous optical 3D printing of green aliphatic polyurethanes, *ACS Appl. Mater. Interfaces*, 2017, **9**, 836–844, DOI: 10.1021/acsami.6b12500.

7 J. Almeida-Pinto, B. S. Moura, V. M. Gaspar and J. F. Mano, Advances in Cell-Rich Inks for Biofabricating Living Architectures, *Adv. Mater.*, 2024, 2313776, DOI: 10.1002/adma.202313776.

8 H. K. Vanyai, F. Prin, O. Guillermin, B. Marzook, S. Boeing, A. Howson, *et al.*, Control of skeletal morphogenesis by the Hippo-YAP/TAZ pathway, *Development*, 2020, **147**, dev187187, DOI: 10.1242/dev.187187.

9 L. Chuwen, Y. Erica, Z. Kuan, J. Xuan, C. Stacey, T.-P. Katherine, *et al.*, YAP is essential for mechanical force production and epithelial cell proliferation during lung branching morphogenesis, *eLife*, 2017, e21130, DOI: 10.7554/eLife.21130.001.

10 Z. Zi and E. Klipp, Cellular signaling is potentially regulated by cell density in receptor trafficking networks, *FEBS Lett.*, 2007, **581**, 4589–4595, DOI: 10.1016/j.febslet.2007.08.047.

11 S. You, Y. Xiang, H. H. Hwang, D. B. Berry, W. Kiratitanaporn, J. Guan, *et al.*, High cell density and high-resolution 3D bioprinting for fabricating vascularized tissues, *Sci. Adv.*, 2023, **9**, eade7923, DOI: 10.1126/sciadv.ade7923.

12 M. Vu, A. Pramanik, A. K. Basak, C. Prakash and S. Shankar, Progress and challenges on extrusion based three dimensional (3D) printing of biomaterials, *Bioprinting*, 2022, **27**, e00223, DOI: **10.1016/j.bprint.2022.e00223**.

13 A. Persaud, A. Maus, L. Strait and D. Zhu, 3D Bioprinting with Live Cells, *Regener. Biomater.*, 2022, **3**, 292–309, DOI: **10.1016/j.engreg.2022.07.002**.

14 T. Boothe, L. Hilbert, M. Heide, L. Berninger, W. B. Huttner, V. Zaburdaev, *et al.*, A tunable refractive index matching medium for live imaging cells, tissues and model organisms, *eLife*, 2017, **6**, e27240, DOI: **10.7554/eLife.27240**.

15 S. You, J. Guan, J. Alido, H. H. Hwang, R. Yu, L. Kwe, *et al.*, Mitigating scattering effects in light-based three-dimensional printing using machine learning, *J. Manuf. Sci. Eng.*, 2020, **142**, 081002, DOI: **10.1115/1.4046986**.

16 P. N. Bernal, M. Bouwmeester, J. Madrid-Wolff, M. Falandt, S. Florczak, N. G. Rodriguez, *et al.*, Volumetric Bioprinting of Organoids and Optically Tuned Hydrogels to Build Liver-Like Metabolic Biofactories, *Adv. Mater.*, 2022, **34**, 2110054, DOI: **10.1002/adma.202110054**.

17 X. Zhang, X. Zhang, Y. Li and Y. Zhang, Applications of Light-Based 3D Bioprinting and Photoactive Biomaterials for Tissue Engineering, *Materials*, 2023, **16**, 7461, DOI: **10.3390/ma16237461**.

18 A. Saad, A. S. Mahdi and I. Nasr, Successful Desensitization to the Radiocontrast Material Iohexol (OmnipaqueTM), *Cureus*, 2022, e32356, DOI: **10.7759/cureus.32356**.

19 J. Baek, H. W. Jeong, Y. J. Heo, S. Yun, M. Kang, B. Kim, *et al.*, Comparison of Safety and Diagnostic Efficacy of Iohexo240 mgI/mL, Iopamidol 250 mgI/mL, and Iodixanol 270 mgI/mL in Cerebral Angiography: A Prospective, Multicenter Study, *Neurointervention*, 2024, **19**, 82–91, DOI: **10.5469/neuroint.2024.00129**.

20 C. Saade, L. Karout, K. El Asmar, L. Naffaa, F. El Merhi, R. Salman, *et al.*, Impact of various iodine concentrations of iohexol and iodixanol contrast media on image reconstruction techniques in a vascular-specific contrast media phantom: quantitative and qualitative image quality assessment, *Radiol. Med.*, 2021, **126**, 221–230, DOI: **10.1007/s11547-020-01253-4**.

21 J. Rappai, J. H. Crabtree, A. Mancini, S. K. Badugu, A. Kaushal and M. E. Gellens, Compatibility and stability of non-ionic iodinated contrast media in peritoneal dialysis solution and safe practice considerations for CT peritoneography, *Peritoneal Dial. Int.*, 2023, **43**, 151–158, DOI: **10.1177/08968608221096562**.

22 M. J. Budoff, H. S. Lee, S. K. Roy and C. Shekar, Efficacy and Safety of Iodixanol in Computed Coronary Tomographic Angiography and Cardiac Catheterization, *J. Cardiovasc. Dev. Dis.*, 2023, **10**, 449, DOI: **10.3390/jcdd10110449**.

23 M. Itoh, K. Nakayama, R. Noguchi, K. Kamohara, K. Furukawa, K. Uchihashi, *et al.*, Scaffold-free tubular tissues created by a bio-3D printer undergo remodeling and endothelialization when implanted in rat aortae, *PLoS One*, 2015, **10**, e0136681, DOI: **10.1371/journal.pone.0136681**.

24 A. Lee, A. R. Hudson, D. J. Shiwarski, J. W. Tashman, T. J. Hinton, S. Yerneni, *et al.*, 3D bioprinting of collagen to rebuild components of the human heart, *Science*, 2019, **6452**, 482–487, DOI: **10.1126/science.aav9051**.

25 A. Kirillova, R. Maxson, G. Stoychev, C. T. Gomillion and L. Ionov, 4D Biofabrication Using Shape-Morphing Hydrogels, *Adv. Mater.*, 2017, **29**, 1703443, DOI: **10.1002/adma.201703443**.

26 L. Zhang, Y. Xiang, H. Zhang, L. Cheng, X. Mao, N. An, *et al.*, A Biomimetic 3D-Self-Forming Approach for Microvascular Scaffolds, *Adv. Sci.*, 2020, **7**, 1903553, DOI: **10.1002/advs.201903553**.

27 Q. Pi, S. Maharjan, X. Yan, X. Liu, B. Singh, A. M. van Genderen, *et al.*, Digitally Tunable Microfluidic Bioprinting of Multilayered Cannular Tissues, *Adv. Mater.*, 2018, **30**, 1706913, DOI: **10.1002/adma.201706913**.

28 X. Zhou, M. Nowicki, H. Sun, S. Y. Hann, H. Cui, T. Esworthy, *et al.*, 3D Bioprinting-Tunable Small-Diameter Blood Vessels with Biomimetic Biphasic Cell Layers, *ACS Appl. Mater. Interfaces*, 2020, **12**, 45904–45915, DOI: **10.1021/acsami.0c14871**.

29 X. Cao, S. Maharjan, R. Ashfaq, J. Shin and Y. S. Zhang, Bioprinting of Small-Diameter Blood Vessels, *Engineering*, 2021, **7**, 832–844, DOI: **10.1016/j.eng.2020.03.019**.

30 G. R. Tryson and A. R. Shultz, Calorimetric Study of Acrylate Photopolymerization, *J. Polym. Sci., Part A-2*, 1979, **17**, 2059–2075, DOI: **10.1002/pol.1979.180171202**.

31 J. R. Conejo-Garcia, F. Benencia, M. C. Courreges, E. Kang, A. Mohamed-Hadley, R. J. Buckanovich, *et al.*, Tumor-infiltrating dendritic cell precursors recruited by a β-defensin contribute to vasculogenesis under the influence of Vegf-A, *Nat. Med.*, 2004, **10**, 950–958, DOI: **10.1038/nm1097**.

32 L. Long, Y. Hu, T. Long, X. Lu, Y. Tuo, Y. Li, *et al.*, Tumor-associated macrophages induced spheroid formation by CCL18-ZEB1-M-CSF feedback loop to promote transcoelomic metastasis of ovarian cancer, *J. Immunotherap. Cancer*, 2021, **9**, e003973, DOI: **10.1136/jitc-2021-003973**.

33 Z. Lin, X. Zhang, M. R. Fritch, Z. Li, B. Kuang, P. G. Alexander, *et al.*, Engineering pre-vascularized bone-like tissue from human mesenchymal stem cells through simulating endochondral ossification, *Biomaterials*, 2022, **283**, 121451, DOI: **10.1016/j.biomaterials.2022.121451**.

34 N. Zhao, A. F. Pessell, N. Zhu and P. C. Searson, Tissue-Engineered Microvessels: A Review of Current Engineering Strategies and Applications, *Adv. Healthc. Mater.*, 2024, **13**, 2303419, DOI: **10.1002/adhm.202303419**.

35 Y. Xiang, K. Miller, J. Guan, W. Kiratitanaporn, M. Tang and S. Chen, 3D bioprinting of complex tissues in vitro: state-of-the-art and future perspectives, *Arch. Toxicol.*, 2022, **96**, 691–710, DOI: **10.1007/s00204-021-03212-y**.

36 T.-Y. Lu, Y. Xiang, M. Tang and S. Chen, 3D Printing Approaches to Engineer Cardiac Tissue, *Curr. Cardiol. Rep.*, 2023, **25**, 505–514, DOI: **10.1007/s11886-023-01881-y**.

37 R. Iwai, T. Tsujinaka and Y. Nakayama, Preparation of Biotubes with vascular cells component by in vivo incubation using adipose-derived stromal cell-exuding multi-microporous molds, *J. Artif. Organs*, 2015, **18**, 322–329, DOI: **10.1007/s10047-015-0848-7**.

38 C. Yu, J. Schimelman, P. Wang, K. L. Miller, X. Ma, S. You, *et al.*, Photopolymerizable Biomaterials and Light-Based 3D Printing Strategies for Biomedical Applications, *Chem. Rev.*, 2020, **120**, 10695–10743, DOI: **10.1021/acs.chemrev.9b00810**.

39 S. You, P. Wang, J. Schimelman, H. H. Hwang and S. Chen, High-fidelity 3D printing using flashing photo-polymerization, *Addit. Manuf.*, 2019, **30**, 100834, DOI: **10.1016/j.addma.2019.100834**.

40 K. Y. Wu, A. Tabari, É. Mazerolle and S. D. Tran, Towards Precision Ophthalmology: The Role of 3D Printing and Bioprinting in Oculoplastic Surgery, Retinal, Corneal, and Glaucoma Treatment, *Biomimetics*, 2024, **9**, 145, DOI: **10.3390/biomimetics9030145**.

41 J. Guan, S. You, Y. Xiang, J. Schimelman, J. Alido, X. Ma, *et al.*, Compensating the cell-induced light scattering effect in light-based bioprinting using deep learning, *Biofabrication*, 2022, **14**, 15011, DOI: **10.1088/1758-5090/ac3b92**.